Talanta 272 (2024) 125780

Contents lists available at ScienceDirect

Talanta

journal homepage: www.elsevier.com/locate/talanta

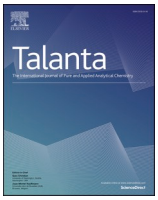

Oxygen vacancies-driven signal enhanced photoelectrochemical sensor for mercury ions detection

Xiang Ren [a], Na Song [a], Jingui Chen [a], Min Gao [a,c,***], Huan Wang [a], Zhong Feng Gao [a], Huangxian Ju [a,d], Jinxiu Zhao [a,b,**], Qin Wei [a,e,*]

[a] Key Laboratory of Chemical Sensing & Analysis in Universities of Shandong, School of Chemistry and Chemical Engineering, University of Jinan, Jinan, 250022, PR China
[b] School of Materials Science and Engineering, University of Jinan, Jinan, 250022, PR China
[c] State Key Laboratory of Biobased Material and Green Papermaking, Qilu University of Technology (Shandong Academy of Sciences), Daxue Rd, Changqing District, Jinan, Shandong, 250353, PR China
[d] Analytical Chemistry for Life Science, School of Chemistry and Chemical Engineering, Nanjing University, Nanjing, 210023, PR China
[e] Department of Chemistry, Sungkyunkwan University, Suwon, 16419, Republic of Korea

ARTICLE INFO

Keywords:
Photoelectrochemistry
$BiVO_{4-x}/Bi_2S_3$
DNA
Hg^{2+}
Oxygen vacancy

ABSTRACT

Mercury ion (Hg^{2+}) poses a serious threat to human health due to its high toxicity. In this study, a smartphone-based photoelectrochemical sensor based on oxygen vacancies (OVs) driven signal enhancement for mercury ion detection was designed. $BiVO_{4-x}/Bi_2S_3$/AuNPs were combined with T−Hg^{2+}−T recognition mode to construct a multi-sandwich photoelectrochemical sensor. On the one hand, the OVs can increase the adsorption of light by the materials and enhance the photocurrent response as well as the superconductivity of Au NPs to accelerate the charge transfer at the electrode interface. On the other hand, the multi-sandwich structure was exploited to increase the binding site of Hg^{2+}, as well as the T−Hg^{2+}−T structure for sensitive recognition of Hg^{2+} and signal amplification. The sensor showed good linearity for Hg^{2+} concentration in the range of 0.1 nM–1.0 μM with a detection limit of 4.8 pM (S/N = 3). Eventually the smartphone-based real-time detection sensor is expected to contribute to the future analysis of heavy metal ions.

1. Introduction

In recent years, the rapid development of industry and agriculture has led to extensive heavy metals pollution. Heavy metals greatly threaten human health through the food chain effect [1]. Mercury ion (Hg^{2+}) is one of the highly toxic heavy metal ions that can be extremely hazardous to human health [2]. The Hg^{2+} can cause damage to the human respiratory system, kidneys, and nervous system when a person is chronically exposed to levels of mercury in excess of those specified (10 nM) [3–7]. Therefore, it is urgent to find a sensitive and stable method to detect Hg^{2+}.

At present, there are many methods for the detection of heavy metal ions such as Hg^{2+}. For example, fluorescence probes, surface-enhanced Raman scattering, and colorimetric methods [8–12]. In recent years, photoelectrochemical (PEC) assays have been attracting increasingly more attention due to their simple operation, low background signals, fast analysis speed, and high sensitivity [13,14]. PEC sensor is widely used to detect disease markers and environmental pollutants [15–19]. Among them, substrate materials with excellent properties are essential for the fabrication of sensors with good optoelectronic properties. Therefore, finding semiconductor materials with excellent properties is one of the key tasks in the construction of sensors.

Bismuth-based materials are widely used because of their high visible light response, good biocompatibility, high stability, non-

* Corresponding author. Key Laboratory of Chemical Sensing & Analysis in Universities of Shandong, School of Chemistry and Chemical Engineering, University of Jinan, Jinan, 250022, PR China.
** Corresponding author. Key Laboratory of Chemical Sensing & Analysis in Universities of Shandong, School of Chemistry and Chemical Engineering, University of Jinan, Jinan, 250022, PR China.
*** Corresponding author. Key Laboratory of Chemical Sensing & Analysis in Universities of Shandong, School of Chemistry and Chemical Engineering, University of Jinan, Jinan, 250022, PR China.
E-mail addresses: shdgaomin@whu.edu.cn (M. Gao), mse_zhaojx@ujn.edu.cn (J. Zhao), sdjndxwq@163.com (Q. Wei).

https://doi.org/10.1016/j.talanta.2024.125780
Received 22 December 2023; Received in revised form 19 January 2024; Accepted 8 February 2024
Available online 13 February 2024

toxicity, and low cost [20,21]. In particular, compounds containing ortho-trivalent bismuth are widely used in photocatalysis and other fields because of their suitable conduction band (CB) and valence band (VB) positions. Their excellent properties will have good application prospects in the field of PEC sensing analysis. Compared with $BiPO_4$, Bi_2MoO_6, and Bi_2WO_6, $BiVO_4$ has a suitable band gap (2.3–2.4 eV), which both absorbs a significant portion of visible light and prevents recombination of electron−hole pairs to some extent, making it an n−type semiconductor material with good photoelectric activity [22–27]. In this study, the synthesized $BiVO_4$ ($BiVO_{4-x}$) with a large number of oxygen vacancies (OVs) further improved its photoactivity and enhanced the photocurrent response. The single bismuth−based semiconductor has good photoelectric response, but still cannot meet the high sensitivity requirements of the sensor. Yang et al. utilized $BiVO_4/Bi_2S_3$ heterojunction for HER2 detection and showed excellent performance [28]. Heterostructures formed by compounding different semiconductor materials provide a faster charge transfer rate and better photocurrent response than a single bismuth−based semiconductor. Therefore, Bi_2S_3 is receiving increasing attention due to its narrow and tunable band gap width (1.3–1.7 eV), wider visible light absorption range, good electron transfer capability, good optoelectronic stability, non−toxicity, and low cost [29,30]. Based on these advantages, $BiVO_{4-x}/Bi_2S_3$ composites have faster charge transfer efficiency than $BiVO_{4-x}$ or Bi_2S_3 alone. At the same time, a stable photocurrent signal is obtained, which provides the basis for the high sensitivity of the sensor. However, traditional detection methods suffer from the problem of false positives due to other ions or organic substances. To solve this problem, DNA with specific base sequences and specific conjugation to Hg^{2+} is used as a detector.

In this work, a PEC sensor constructed based on multi−sandwich chain structures can achieve real−time detection of Hg^{2+}. In particular, DNA−I with Au NPs forms Au–S, which acts as an anchor. In this work, thymine-rich DNA−M was used as the recognition strand for Hg^{2+}, which was sensitively recognized by forming a T−Hg^{2+}−T structure [31,32]. The DNA−M and DNA−B recognize and amplify each other on the electrode surface, forming multi−sandwich chain structures. Allowing a large amount of DNA−M to be immobilized on the electrode surface greatly enhances the detection range and sensitivity of the sensor. Furthermore, a smartphone−controlled miniaturized electrochemical workstation allows on−site detection of Hg^{2+}. This work proposes a new sensitive method for Hg^{2+} detection, which is expected to be the future direction of detection.

2. Experimental part

2.1. Reagents and apparatus are reported in supplementary material

2.1.1. Preparation of $BiVO_{4-x}$

The $BiVO_{4-x}$ was synthesized based on the hydrothermal method according to a reported literature with some modifications [33]. Firstly, a homogeneous solution was obtained by ultrasonicating a mixture of 0.6468 g of $Bi(NO_3)_3{\cdot}5H_2O$, 4.0 g of polyvinylpyrrolidone (PVP), and 100 mL of ethylene glycol after 25 min. Subsequently, 0.2400 g of $NaVO_3$ was dissolved in 60 mL of ultrapure water and ultrasonicated for 10 min to obtain a solution. The above solutions were then mixed well under vigorous stirring conditions. Next, the above−mixed solution was transferred to a stainless-steel autoclave with Teflon lining and reacted for 10 h at 180 °C. After cooling, the resulting product solution was alternately centrifuged using ultrapure water and absolute ethanol. Finally, the final product was dried in a vacuum drying oven at 60 °C for 10 h to obtain the final product.

2.2. Preparation of $BiVO_{4-x}/Bi_2S_3$

$BiVO_{4-x}/Bi_2S_3$ was synthesized in situ concerning the reported synthesis of $BiVO_{4-x}/Bi_2S_3$ composites [33]. A mixture of 120 mg of $BiVO_{4-x}$, 2.0 g of PVP, and 80 mL of ultrapure water was ultrasonicated for 25 min to obtain a homogeneous solution. Dissolving 0.5200 g of $Na_2S{\cdot}9H_2O$ in 80 mL of ultrapure water to obtain a solution. After mixing the above solutions well, the solution was transferred to a stainless-steel autoclave with Teflon lining and reacted at 150 °C for 8 h. After cooling, washing and centrifuging the resulting product solution alternately using ultrapure water and absolute ethanol. At the end of the experiment, the final product was dried in a vacuum oven at 60 °C overnight.

2.3. Preparation of Au NPs

Au NPs were synthesized with modifications from the reported literature [34]. 50 μL of $HAuCl_4$ (2 wt%) was dispersed in 10 mL of ultrapure water and preheated to 100 °C. The 0.0500 g of sodium citrate was dispersed in 4.95 mL of ultrapure water to form a solution, which was rapidly injected into the $HAuCl_4$ solution and then reacted for 30 min in an oil bath at 100 °C. After the reaction was finished and cooled to room temperature, centrifugation was performed to collect the Au NPs.

2.4. Construction of multi-sandwich chain structure PEC sensor

The PEC sensor was constructed as shown in Scheme 1. Firstly, 30 μL $BiVO_{4-x}/Bi_2S_3$ compound (4.1 mg/mL) was dropwise applied to the ITO and dried at room temperature. Next, 10 μL Au NPs solution was modified onto the ITO/$BiVO_{4-x}/Bi_2S_3$ surface and dried at 50 °C to acquire ITO/$BiVO_{4-x}/Bi_2S_3$/Au. Then, 20 μL (1.0 μM) of DNA−I modified with sulfhydryl groups was dropwise added to the above electrode surface, and incubated in a refrigerator at 4 °C for 1 h. Then, 20 μL (1.0 μM) of DNA−M was modified on the electrode surface and incubated in a refrigerator at 4 °C for 1 h. Finally, 20 μL (1.0 μM) of DNA−B solution was modified on the electrode surface and incubated in a refrigerator at 4 °C for 1 h. After allowing it to dry naturally, the sensor construction was completed.

3. Results and discussion

3.1. Characterization of $BiVO_{4-x}$, Bi_2S_3, $BiVO_{4-x}/Bi_2S_3$, and Au NPs

Scanning electron microscopy (SEM) was used to analyze the morphology of $BiVO_{4-x}$, Bi_2S_3, and $BiVO_{4-x}/Bi_2S_3$. As shown in Fig. 1A, $BiVO_{4-x}$ is nanosphere with a size of about 500 nm. Fig. 1B presents the morphology of Bi_2S_3, it is a regular one−dimensional nanorod−like morphology with a length of about 100 nm. The SEM image of $BiVO_{4-x}/Bi_2S_3$ is shown in Fig. 1C, which is a nanospherical structure with a defective and porous surface. As shown in Figure S1, the four elements Bi, S, V, and O are distributed in $BiVO_{4-x}/Bi_2S_3$. From the mapping image of Figure S2, it can be shown that the four elements Bi, S, V, and O are homogeneously distributed in the compounds. The morphology and size of the synthesized Au NPs were investigated by transmission electron microscopy (TEM), where the size of the Au NPs can be seen to be around 10 nm (Fig. 1D). These morphological characterizations further demonstrate the successful synthesis of $BiVO_{4-x}/Bi_2S_3$ and Au NPs.

The phase composition and crystal structures of $BiVO_{4-x}$, Bi_2S_3, and $BiVO_{4-x}/Bi_2S_3$ were analyzed by X−ray diffraction (XRD) patterns. As shown in Fig. 2A, the synthesized $BiVO_{4-x}$ diffracted strong peaks at (020) and (110) crystal plane. XRD peaks match those of its standard card (JCPDS No. 14−0688) and there are no stray peaks. The synthesized Bi_2S_3 diffracts intense peaks at the (130), (310), and (211) crystal planes. And there are no stray peaks, which can match the standard card (JCPDS No. 17−0320) of Bi_2S_3 perfectly. The diffraction peak of the composite diffracts a stronger peak at 24.7° than the peak of Bi_2S_3, which may be responsible for the formation of heterojunctions. These results demonstrate the successful synthesis of $BiVO_{4-x}$, Bi_2S_3, and $BiVO_{4-x}/Bi_2S_3$.

Using X−ray photoelectron spectroscopy (XPS) to analyze the

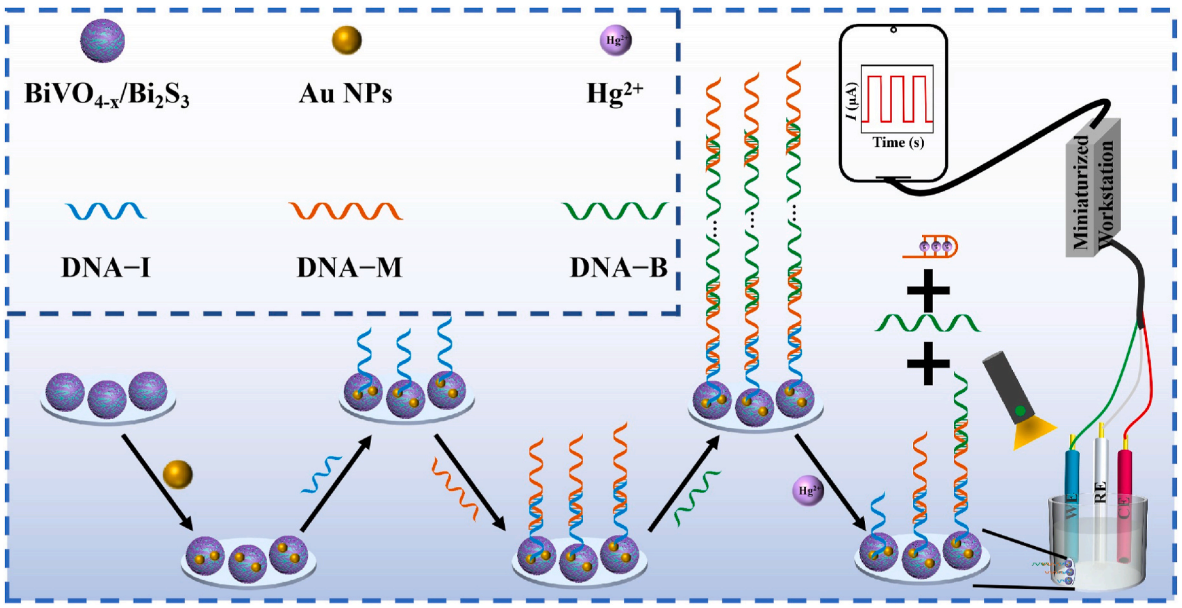

Scheme 1. The construction process of the PEC sensor.

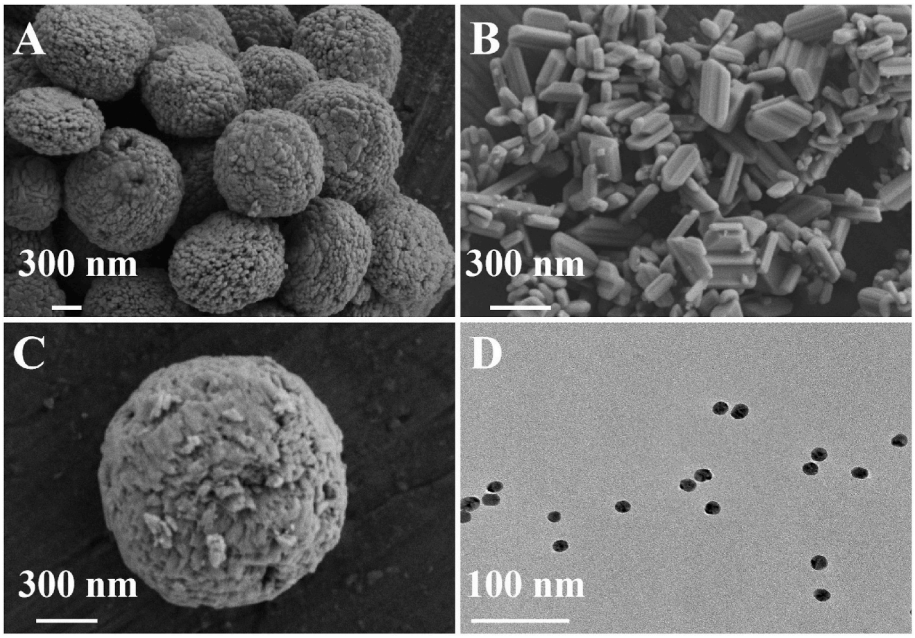

Fig. 1. (A) SEM of $BiVO_{4-x}$, (B) SEM of Bi_2S_3, (C) SEM of $BiVO_{4-x}/Bi_2S_3$, (D) TEM of Au NPs.

elemental composition of the composites and the valence states of each element. Fig. 2B is the XPS full spectrum of $BiVO_{4-x}/Bi_2S_3$ [35]. Fig. 2C displays the high-resolution energy spectrum of O 1s with binding energies of 528.78 eV and 530.08 eV for lattice oxygen (V–O) and surface oxygen (O–H), respectively. Fig. 2D shows the high−resolution XPS of Bi 4f, where 157.28 eV and 162.58 eV correspond to Bi $4f_{7/2}$ and Bi $4f_{5/2}$ in $BiVO_{4-x}$ respectively, and 157.88 eV and 163.28 eV correspond to Bi $4f_{7/2}$ and Bi $4f_{5/2}$ in Bi_2S_3, respectively. These results demonstrate the presence of Bi^{3+} in the complexes. As shown in Fig. 2E, the peaks binding energy of S 2p are located at 159.88 eV and 161.18 eV, corresponding to S $2p_{3/2}$ and S $2p_{1/2}$, respectively, proving the existence of S^{2-}. The high-resolution spectrum of V 2p is shown in Fig. 2F, where 515.68 eV and 523.28 eV are the peak binding energies of V $2p_{3/2}$ and V $2p_{1/2}$, respectively, proving the existence of V^{5+}. These results indicate the successful synthesis of $BiVO_{4-x}/Bi_2S_3$ composites.

An electron paramagnetic resonance (EPR) spectroscopy study was carried out to demonstrate the presence of OVs. As shown in Fig. 3A, there is a distinct EPR signal centered at g = 2.002, which was ascribed to electrons trapped on the OVs [36]. Fig. 3B shows the current comparison with and without OVs in $BiVO_4$. The photocurrent of the composite without OVs is 26.9 μA, but when OVs are included, the photocurrent of the composite reaches 44.9 μA, which is increased by 66.9%.

3.2. Comparison of photocurrent signals

To verify the successful construction of the sensor, photocurrent comparison experiments (Fig. 4A) were performed during the layered modification of the sensor. In which, the photocurrent of the electrode with only modified substrate material was stable at around 44.9 μA

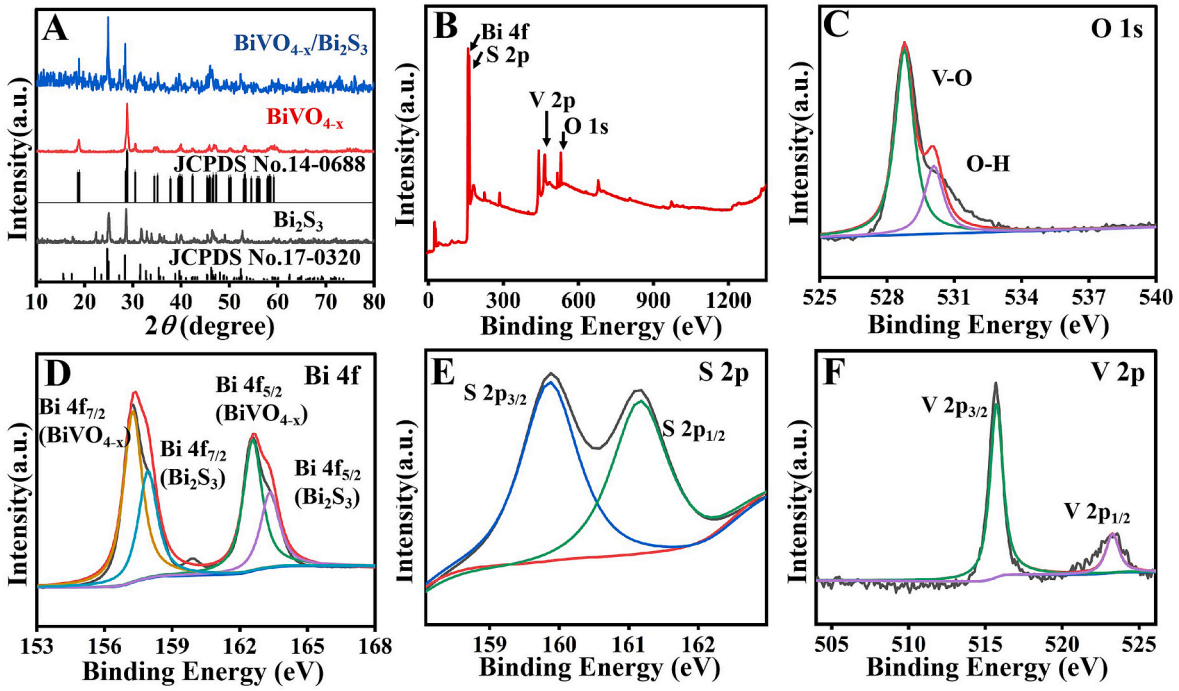

Fig. 2. (A) XRD of $BiVO_{4-x}$, Bi_2S_3 and $BiVO_{4-x}/Bi_2S_3$, (B) X−ray photoelectron spectroscopy of $BiVO_{4-x}/Bi_2S_3$ composites, (C) O 1s, (D) Bi 4f, (E) S 2p, (F) V 2p.

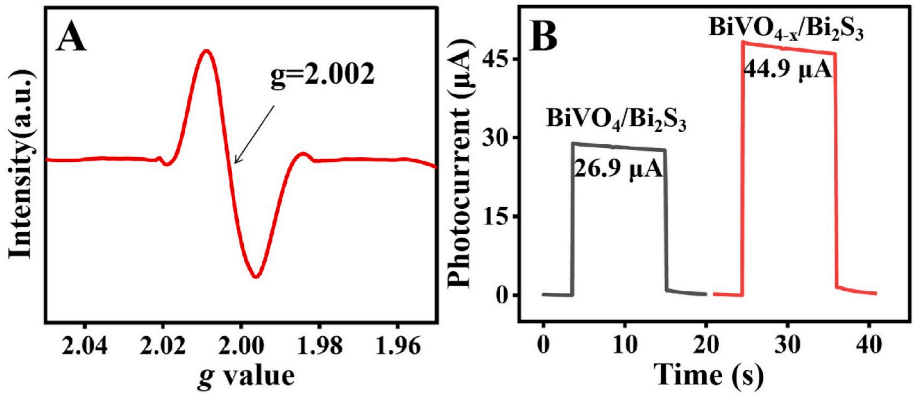

Fig. 3. (A) EPR of $BiVO_{4-x}$, (B) the photocurrent comparison of substrate material (4.1 mg/mL) with and without oxygen vacancies.

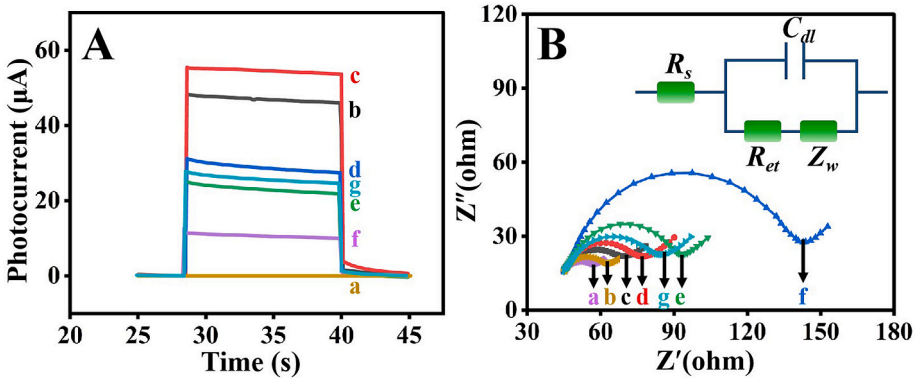

Fig. 4. (A) Photocurrent responses and (B) EIS of (a) ITO, (b) ITO/$BiVO_{4-x}/Bi_2S_3$, (c) ITO/$BiVO_{4-x}/Bi_2S_3$/Au, (d) ITO/$BiVO_{4-x}/Bi_2S_3$/Au/DNA−I, (e) ITO/$BiVO_{4-x}/Bi_2S_3$/Au/DNA−I/DNA−M, (f) ITO/$BiVO_{4-x}/Bi_2S_3$/Au/DNA−I/DNA−M/DNA−B, (g) ITO/$BiVO_{4-x}/Bi_2S_3$/Au/DNA−I/DNA−M/DNA−B/Hg^{2+} in 0.1 M pH 7.6 PBS containing 0.1 M AA (A) and 0.1 M KCl containing 2.5 mM $[Fe(CN)_6]^{4-/3-}$ (B).

(curve b). Since the $BiVO_{4-x}/Bi_2S_3$ heterojunction can provide a stable photocurrent output. As the excellent conductivity of Au NPs, when they were modified on the surface of the substrate material, it resulted in an increase of photocurrent to 51.2 μA (curve c). Due to the poor conductivity of DNA molecules, the photocurrent obtained decreased significantly to about 26.5 μA when DNA−I was further modified on the electrode surface (curve d). The spatial site resistance is further increased when the modified DNA−M is on the electrode due to the ability of DNA−M and DNA−I to recognize each other for pairing. This resulted in a decrease in photocurrent to 21.4 μA (curve e). Finally, after DNA−B and DNA−M recognized each other by pairwise amplification, multi−sandwich strand structures were formed. The spatial site resistance increased to a maximum, leading to a further reduction of the photocurrent to 9.45 μA (curve f). The photocurrent increased to 23.8 μA (curve g) when Hg^{2+} at a concentration of 1.0 μM was detected with the above−constructed sensor. Due to the presence of Hg^{2+}, which can be specifically recognized with DNA−M to form T−Hg^{2+}−T structures. This causes DNA−B and DNA−M to detach from the sensor surface, decreasing spatial site resistance and increasing the photocurrent. In conclusion, the comparison of photocurrents after layer modification indicates that the construction of the sensor was successful.

3.3. Comparison of the electrochemical impedance spectroscopy

To verify the success of the layer−by−layer modification process during sensor construction, electrochemical impedance spectroscopy (EIS) is a commonly used characterization method. The open circuit voltage is 0.18 V, the frequency is 0.1–1 × 10^5 Hz, the amplitude is 5 mV, and $[Fe(CN)_6]^{4-/3-}$ of 2.5 mM is used as the detection solution. The equivalent circuit at the electrolyte−electrode interface is shown in the inset of Fig. 4B, which contains the electrolyte impedance (R_s), electrode interface resistance (R_{et}), and double−layer capacitance (C_{dl}). The specific data obtained by combining the software fits are in Table S1. As shown in Fig. 3B, the impedance of the electrode modified with $BiVO_{4-x}/Bi_2S_3$ (curve b, 17.37 Ω) is greater than the impedance of the naked ITO (curve a, 13.7 Ω), which proves that $BiVO_{4-x}/Bi_2S_3$ was successfully modified on the ITO surface. When a layer of Au NPs was modified on the surface of $BiVO_{4-x}/Bi_2S_3$, the impedance value increased to 25.58 Ω (curve c). It indicates that the formation of Au–S increases the spatial site resistance. The impedance of the electrode increases to 31.47 Ω when DNA−I was modified as shown in curve d. Since DNA−I acts as a biomolecule resulting in a larger spatial site resistance of the electrode. This indicates that the sulfhydryl group and Au NPs successfully formed Au–S. When DNA−M was paired with DNA−I specific recognition led to a further increase in spatial site resistance. These result in an increase in sensor impedance to 45.66 Ω (curve e). DNA−B and DNA−M were amplified in large quantities on the electrode surface after mutual recognition. This increased the spatial site resistance of the electrode to a maximum, increasing in impedance to 92.72 Ω (curve f). The impedance decreased to 38.04 Ω (curve g) when the constructed sensor was used to detect Hg^{2+} at a concentration of 1.0 μM. The formation of the T−Hg^{2+}−T structures resulted in the detachment of DNA−M and DNA−B from the electrode surface. This resulted in a reduction of spatial site resistance and accelerated charge transfer. The above results show that the modification at the sensor layer by layer is successful.

3.4. Electron transport mechanism

Fig. 5 shows a possible electron transfer mechanism for a PEC sensor. The band gap values of $BiVO_{4-x}$ and Bi_2S_3 are 2.38 eV and 1.32 eV, respectively, which are obtained by solid ultraviolet diffuse reflection (Figures S3A and S3C). The E_{fb} of Bi_2S_3 and $BiVO_{4-x}$ were obtained by Mott-Schottky test (Figures S3B and S3D) as −0.14 eV vs. SCE (0.1 eV vs. NHE) and −0.04 eV vs. SCE (0.2 eV vs. NHE), respectively. The E_{CB} of n−type semiconductors is 0–0.2 eV lower than E_{fb}. Therefore, the E_{CB} of Bi_2S_3 and $BiVO_{4-x}$ are −0.1 eV (vs. NHE) and 0 eV (vs. NHE), respectively. Combining the band gap values (E_g) obtained from solid-state UV tests and the equation $Eg = E_{VB} - E_{CB}$, the valence band potentials (E_{VB}) of Bi_2S_3 and $BiVO_{4-x}$ were calculated to be 1.22 eV (vs. NHE) and 2.38 eV (vs. NHE), respectively. When light is irradiated to the working electrode, the electron−hole pairs of $BiVO_{4-x}$ and Bi_2S_3 are excited and separated in the VB. The photogenerated electrons are transferred to the CB position of Bi_2S_3 via Au NPs and the holes are transferred to the VB of Bi_2S_3. This stepped energy level position (the CB of Bi_2S_3 is higher than the CB position of $BiVO_{4-x}$) leads to a rapid transfer of electrons in the CB of Bi_2S_3 to the CB of $BiVO_{4-x}$ and ultimately to the ITO. At the same time, the holes in the VB of $BiVO_{4-x}$ are transferred to the VB of Bi_2S_3. In addition, the negative charge provided by the electrolyte ascorbic acid (AA) traps the photogenerated holes. Therefore, the $BiVO_{4-x}/Bi_2S_3$ heterojunction can effectively inhibit the recombination of electron-hole pairs and accelerate the electron transfer rate.

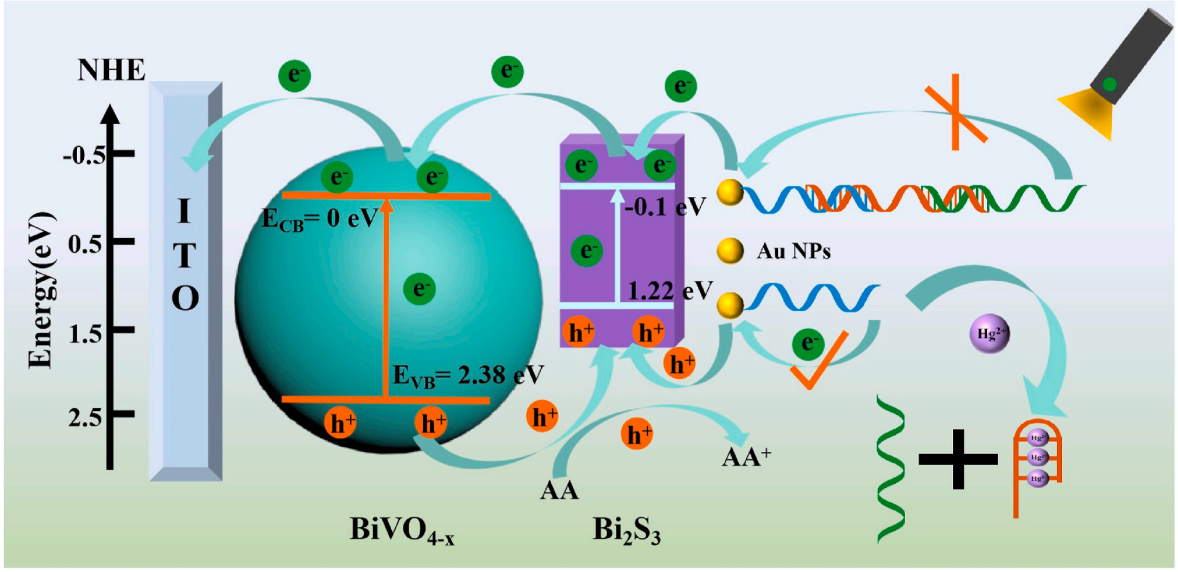

Fig. 5. Diagram of the possible mechanism of the sensor in 0.1 M pH 7.6 PBS containing 0.1 M AA.

3.5. Electrochemical active surface area

The electroactive surface area of the electrode affects the amount of DNA loaded on the electrode surface, with a consequent effect on the performance of the sensor. Cyclic voltammetry (CV) tests were performed on bare ITO (Fig. 6A) and ITO/$BiVO_{4-x}/Bi_2S_3$ (Fig. 6C). All the analyses are based on the Randles Sevcik equation $I = 2.69 \times 10^5\, A\, D^{1/2}\, n^{3/2}\, v^{1/2}\, c$, where I is the peak current as a function of scanning rate, A is the electroactive surface area (cm^2), D (6.70×10^{-6} cm^2/s) is the diffusion coefficient of $[Fe(CN)_6]^{4-/3-}$, $n = 1$ is the number of electrons transferred during redox, v is the scanning rate (V/s), and c is the concentration (5 mM) of $[Fe(CN)_6]^{4-/3-}$. The potential range was set to −0.2–0.6 V, the scanning rate was increased sequentially from 0.02 V/s to 0.20 V/s at intervals of 0.02 s, and 5 mM $[Fe(CN)_6]^{4-/3-}$ was employed as the electrolyte solution. The formulas for ITO/$BiVO_{4-x}/Bi_2S_3$ and bare ITO are $I = 2604.5 \times v^{1/2} + 25.6$ ($R^2 = 0.99$) (Fig. 6D) and $I = 2057.9 \times v^{1/2} + 9.77$ ($R^2 = 0.99$) (Fig. 6B), respectively. The electroactive surface area of the bare ITO and ITO/$BiVO_{4-x}/Bi_2S_3$ are 0.59 cm^2 and 0.75 cm^2, respectively. The modification of $BiVO_{4-x}/Bi_2S_3$ increased the electrode electroactive surface by 27.1% and thus would further increase the loading of DNA on the electrode surface.

3.6. Optimal conditions selection

To ensure the best performance of the constructed PEC sensor, the concentration of $BiVO_{4-x}/Bi_2S_3$, the pH of the solution, and the concentration of AA were optimized by Box-Behnken experiments. As shown in Fig. 6, substrate concentrations varied from 3.5 mg/mL to 4.5 mg/mL, pH from 7.0 to 7.8, and AA concentrations from 0.08 M to 0.12 M. Using Design Expert software to simulate the analysis data, the resulting equation is I (μA) $= -118.27687 + 11.94750A + 170.81250B + 28.15937C + 3.75AB + 0.0125AC - 0.625BCE - 1.53A^2 - 950B^2 - 1.90625C^2$, where A is the concentration of $BiVO_{4-x}/Bi_2S_3$, B is the concentration of AA, and C is pH. The best experimental conditions obtained were as follows when the concentration of $BiVO_{4-x}/Bi_2S_3$ was 4.1 mg/mL, the pH value was 7.6, the concentration of AA was 0.1 M, and the maximum photocurrent value was 18.1 μA. The resulting 3D simulation images are shown in Fig. 7. Where the interaction between the two factors is explained by the shape of the bottom contour. When tending to be circular, it indicates that there is no significant interaction between the two. Conversely, when tending to be elliptical, it indicates a significant interaction between the two factors. Fig. 7 displays that the bottom contours tend to be circular, which proves that there is no significant interaction between the two pairs of the three preferred experimental conditions.

3.7. Performance of the PEC sensor

Under optimal experimental conditions, the performance of the constructed PEC sensor was tested. As shown in Fig. 8A, the photocurrent intensity increases as the Hg^{2+} concentration (0.1 nM–1.0 μM) gradually increases. Fig. 8B shows the linear relationship between the intensity of the photocurrent and the logarithm of Hg^{2+} concentration (c, nM, 0.1 nM to 1.0 μM) with the linear equation $I = 2.68 \lg c + 15.62$ ($R^2 = 0.998$, 95% confidence interval) with a detection limit of 4.8 pM (S/N = 3). As shown in Table S2, the PEC sensor constructed in this work has a wider detection range and lower detection limit compared to other methods.

The stability of the PEC sensor is the prerequisite for Hg^{2+} sensitive detection. The photocurrent stability and storage stability of the sensor were tested. As shown in Fig. 8C, the photocurrent remained 90.4% of the initial current after switching the light on and off to irradiate the light 12 times, with an RSD of 3.1%. After storing the PEC sensor incubated with DNA in a refrigerator at 4 °C for 1 week, 2 weeks, 3 weeks, 4 weeks, and 5 weeks, respectively. The photocurrent intensities obtained were 98.3%, 96.6%, 95.4%, 94.1%, and 92.4% of the initial photocurrent, respectively, indicating that the constructed PEC sensor had good storage stability (Fig. 8E).

The selectivity of the PEC sensor is investigated by detecting other heavy metal ions (Pb^{2+}, Cd^{2+}, Cr^{6+}, Cu^{2+}, Mn^{4+}) that may coexist with

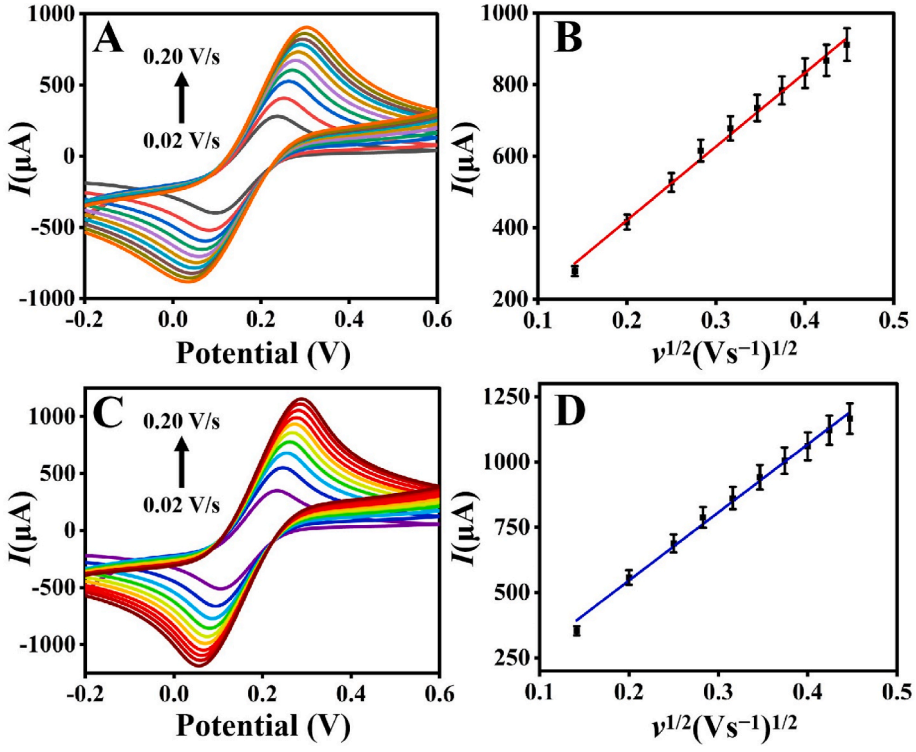

Fig. 6. (A, C) Cyclic voltammograms of ITO (A) and ITO/$BiVO_{4-x}/Bi_2S_3$ (4.1 mg/mL, 30 μL) (C) in 0.1 M KCl containing 5 mM $[Fe(CN)_6]^{4-/3-}$ at different scanning rates, and (B, D) the corresponding plots of anodic peak current to $v^{1/2}$ (error bar = SD, n = 3).

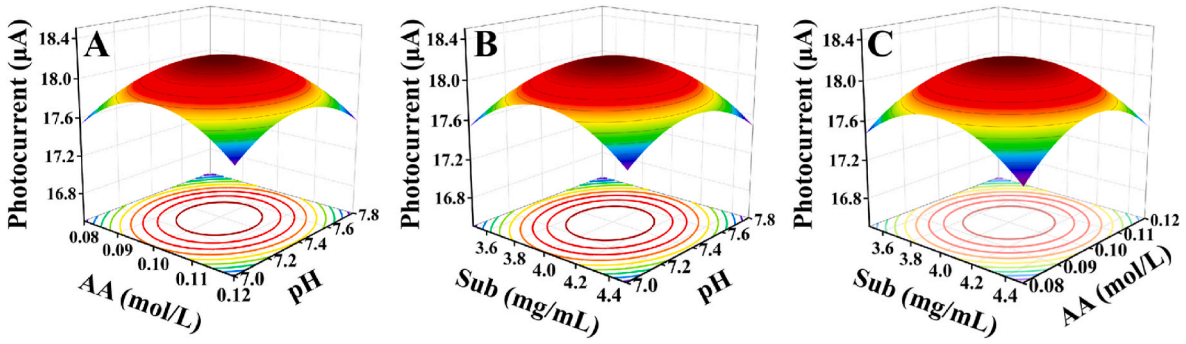

Fig. 7. Box–Behnken experiment for AA concentration, pH, and substrate concentration, 3D diagrams of the interaction between the two factors (A, B, C).

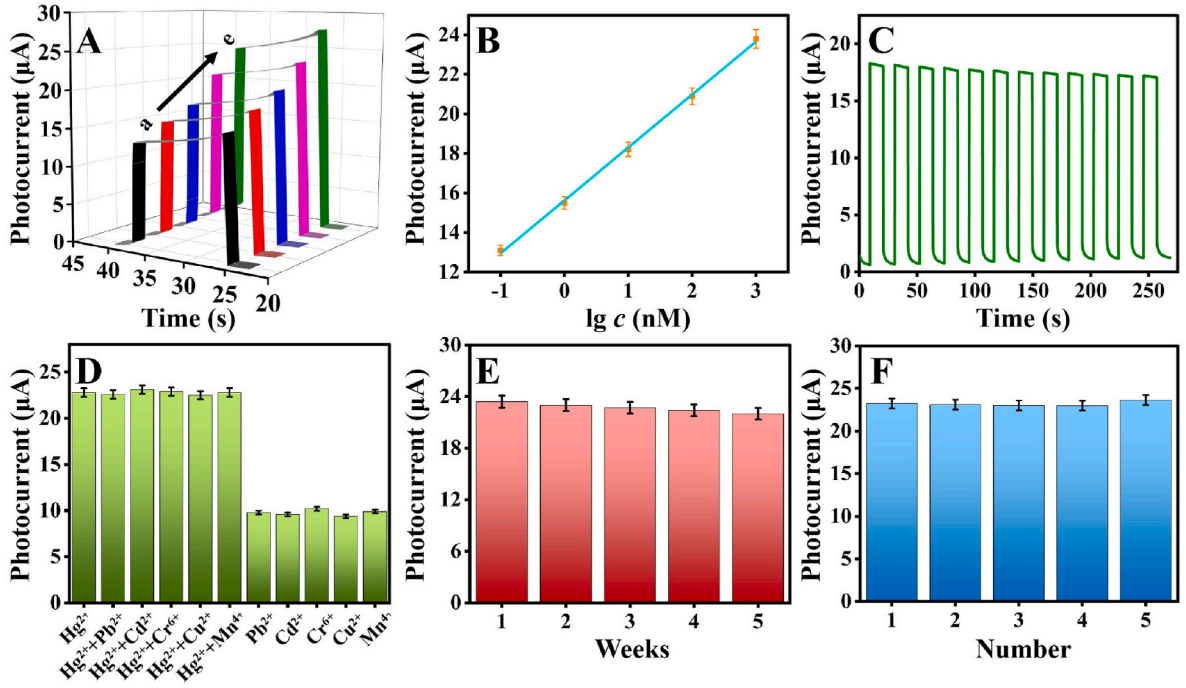

Fig. 8. (A) Photocurrent variation curves at different Hg^{2+} concentrations, (a) 10^{-10} M, (b) 10^{-9} M, (c) 10^{-8} M, (d) 10^{-7} M, (e) 10^{-6} M, (B) logarithmic calibration plot of the sensor at different concentrations of Hg^{2+} (error bar = SD, n = 5), (C) stability of sensor in 10^{-8} M Hg^{2+}, (D) selectivity of sensor in 10^{-6} M Hg^{2+} (error bar = SD, n = 3), (E) storage stability of sensor in 10^{-6} M Hg^{2+} (error bar = SD, n = 3), (F) repeatability of sensor in 10^{-6} M Hg^{2+} (error bar = SD, n = 3).

Hg^{2+}. As shown in Fig. 8D, the photoelectric response of Pb^{2+}, Cd^{2+}, Cr^{6+}, Cu^{2+}, Mn^{4+}, and other heavy metal ions was still displayed as blank electrodes. However, when Hg^{2+} and each of the above five ions were mixed in equal amounts and detected, there was a significant photoelectric response. In conclusion, it demonstrated that the constructed PEC sensor has good selectivity for Hg^{2+}.

The repeatability of the PEC sensor is one of the most important indexes for evaluating the sensors, which is an important prerequisite for ensuring the precision of the detection results. Under the optimal experimental conditions, five identical sensors were prepared simultaneously to detect Hg^{2+} at a concentration of 1.0 μM. As shown in Fig. 8F, the photocurrent values of 23.24 μA, 23.10 μA, 23.02 μA, 22.98 μA, and 23.65 μA, respectively, and the relative standard deviation (RSD) obtained was 1.2%. Indicating that the constructed PEC sensors have good repeatability.

In addition, the reproducibility of the sensor (Figure S4) is another important indicator for evaluating the sensor. It is a prerequisite for assessing the accuracy of the sensor. Five sets of experiments were conducted in different environments, and the measured photocurrent values were 23.00 μA, 22.80 μA, 24.10 μA, 24.30 μA, and 22.70 μA, with an RSD of 3.3%. It demonstrated that the constructed sensors have good reproducibility.

3.8. Sample analysis

To verify the accuracy of the constructed sensor in the actual sample, the standard addition recovery method was used to detect the water of Jiazi Lake and the tap water of the laboratory respectively. The

Table 1
Analysis of actual samples containing Hg^{2+}.

Sample	Added (ng/mL)	Found (ng/mL)	Recovery (n = 5, %)	RSD (n = 5, %)
Lake water	0	0.51		2.2
	0.50	0.99	96.0	2.4
	1.00	1.53	102.0	3.0
	1.50	2.06	103.0	3.1
Tap water	0	0.13		1.2
	0.30	0.41	93.3	1.3
	0.40	0.52	97.5	1.6
	0.50	0.65	104.0	2.3

detection results are shown in Table 1, with recoveries in the range of 93.3%–104.0% and RSD in the range of 1.2%–3.1%. Indicating that the constructed sensors have good precision and practical application.

4. Conclusion

In conclusion, a novel PEC sensor for Hg^{2+} detection based on $BiVO_{4-x}/Bi_2S_3$ and a multi-sandwich chain structure was successfully constructed. The $BiVO_{4-x}/Bi_2S_3$ complexes with good visible light absorption ability was used as a photoactive substance to accelerate the electron transfer and inhibit the recombination of electron−hole pairs, increasing the photocurrent signal. In addition, the formation of multi−sandwich chain structures broadens the linear range and improves sensitivity. The sensor has good selectivity, stability, repeatability, reproducibility, and a wide linearity range from 0.1 nM to 1.0 μM with a low detection limit of 4.8 pM (S/N = 3). The PEC sensor designed in this work enables real−time detection of Hg^{2+} through smartphone control. This greatly improves efficiency and saves the detection cost. However, the detection mode of the three−electrode system has problems such as low degree of portability and integration, which can be solved by preparing a more portable microfluidic sensing chip. Given the above advantages, the sensor can be used for the detection of heavy metal ions and will have a wider application in the field of analytical chemistry in the future.

CRediT authorship contribution statement

Xiang Ren: Writing – review & editing, Funding acquisition. **Na Song:** Writing – original draft. **Jingui Chen:** Methodology, Data curation. **Min Gao:** Formal analysis. **Huan Wang:** Writing – review & editing, Methodology. **Zhong Feng Gao:** Formal analysis. **Huangxian Ju:** Writing – review & editing, Formal analysis. **Jinxiu Zhao:** Methodology. **Qin Wei:** Funding acquisition.

Declaration of competing interest

The authors declare that they have no known competing financial interests or personal relationships that could have appeared to influence the work reported in this paper.

Data availability

Data will be made available on request.

Acknowledgments

This study was supported by the National Natural Science Foundation of China (No. 22204059, No. 22204060, No. 22264025), the Natural Science Foundation of Shandong Province (No. ZR2021QB120, ZR2022QB021), the Foundation of Yunnan Key Laboratory of Rural Energy Engineering (Yunnan Normal University), the Special Foundation for Taishan Scholar Professorship of Shandong Province (Prof. Q. Wei), Talent Introduction and Training Program for Youth Innovation teams in Colleges and universities of Shandong Province, Postdoctoral Research Start-up Foundation from the University of Jinan (No. XBH2202).

Appendix A. Supplementary data

Supplementary data to this article can be found online at https://doi.org/10.1016/j.talanta.2024.125780.

References

[1] Y. Su, L. Su, B. Liu, Y. Lin, D. Tang, Self-powered photoelectrochemical assay for Hg^{2+} detection based on g-C_3N_4-CdS-CuO composites and redox Cycle signal amplification Strategy, Chemosensors 10 (7) (2022) 286, https://doi.org/10.3390/chemosensors10070286.
[2] R. Xie, Y. Qu, M. Tang, J. Zhao, S. Chua, T. Li, F. Zhang, E.H.W. A, F. Chai, Carbon dots-magnetic nanocomposites for the detection and removal of Hg(II), Food Chem. 364 (2021) 130366, https://doi.org/10.1016/j.foodchem.2021.130366.
[3] L. Yu, Y. Qu, F. Chai, L. Chen, Facile preparation of highly sensitive and selective fluorescent paper sensor for the visual and cyclic detection of Cu^{2+} and Hg^{2+}, New J. Chem. 42 (21) (2018) 17478–17485, https://doi.org/10.1039/c8nj03550d.
[4] K. Abbas, H. Znad, M.R. Awual, A ligand anchored conjugate adsorbent for effective mercury(II) detection and removal from aqueous media, Chem. Eng. J. 334 (2018) 432–443, https://doi.org/10.1016/j.cej.2017.10.054.
[5] Y. Wang, L. Zhang, X. Han, L. Zhang, X. Wang, L. Chen, Fluorescent probe for mercury ion imaging analysis: strategies and applications, Chem. Eng. J. 406 (2021) 127166, https://doi.org/10.1016/j.cej.2020.127166.
[6] A.N. Vijayan, Z. Liu, H. Zhao, P. Zhang, Nicking enzyme-assisted signal-amplifiable Hg^{2+} detection using upconversion nanoparticles, Anal. Chim. Acta 1072 (2019) 75–80, https://doi.org/10.1016/j.aca.2019.05.001.
[7] S. Ma, Q. Zhang, J. Zhu, H. Shi, K. Zhang, Y. Shen, Rational engineering of Ag-doped reduced graphene oxide as electrochemical sensor for trace mercury ions monitoring, Sens. Actuators, B 345 (2021) 130383, https://doi.org/10.1016/j.snb.2021.130383.
[8] Z. Lu, M. Chen, T. Liu, C. Wu, M. Sun, G. Su, X. Wang, Y. Wang, H. Yin, X. Zhou, J. Ye, Y. Shen, H. Rao, Machine Learning system to monitor Hg^{2+} and sulfide using a polychromatic fluorescence-colorimetric paper sensor, ACS Appl. Mater. Interfaces (2023), https://doi.org/10.1021/acsami.2c16565.
[9] R. Nakatani, S. Biswas, T. Irie, Y. Niihori, S. Das, Y. Negishi, Unlocking the potential of an atom-precise Ag_{12} cluster assembled material as a highly efficient SERS sensor for the detection of Hg^{2+} ions, ACS Mater. Lett. (2023) 438–445, https://doi.org/10.1021/acsmaterialslett.3c01198.
[10] J. Yang, L. Feng, J. Liu, S. Li, N. Li, X. Zhang, DNA-mediated charge neutralization of AuNPs for colorimetric sensing of Hg^{2+} in environmental waters and cosmetics, Sens. Actuators, B 398 (2024), https://doi.org/10.1016/j.snb.2023.134697.
[11] Z.-g. Liu, M. Xiao, R.-z. Yang, Q.-q. Zhou, H.-f. Ye, C.-q. Yi, Multiplexed detection of Fe^{3+}, cobalamin and folate using fluorescent nanoprobe-based microarrays and a smartphone, Journal of Analysis and Testing 5 (1) (2021) 19–29, https://doi.org/10.1007/s41664-021-00163-2.
[12] S. Chen, C. Chen, J. Wang, F. Luo, L. Guo, B. Qiu, Z. Lin, A bright nitrogen-doped-carbon-dots based fluorescent biosensor for selective detection of copper ions, Journal of Analysis and Testing 5 (1) (2021) 84–92, https://doi.org/10.1007/s41664-021-00162-3.
[13] R. Xiao, H. Yu, M. Liu, W. Xu, Y. Qin, R. Tan, Y. Chen, J. Wen, X. Peng, W. Gu, C. Zhu, L. Hu, Selective chemical reactivity of non-fullerene acceptor for photoelectrochemical bioassay of urease activity, Adv. Funct. Mater. (2023), https://doi.org/10.1002/adfm.202304915.
[14] Q. Zhang, Y. Fu, K. Xiao, C. Du, X. Zhang, J. Chen, Sensitive dual-mode biosensors for CYFRA21-1 assay based on the dual-signaling electrochemical ratiometric strategy and "On-Off-On" PEC method, Anal. Chem. 93 (17) (2021) 6801–6807, https://doi.org/10.1021/acs.analchem.1c00746.
[15] J. Zhang, X. Xue, Y. Du, J. Zhao, H. Ma, X. Ren, Q. Wei, H. Ju, Antigen-down PEC immunosensor for CYFRA21-1 detection based on photocurrent polarity switching strategy, Anal. Chem. 94 (36) (2022) 12368–12373, https://doi.org/10.1021/acs.analchem.2c01478.
[16] J. Chen, J. Zhao, J. Feng, D. Wu, H. Ma, X. Ren, Q. Wei, H. Ju, Photoelectrochemical immunosensor based on a 1D Fe_2O_3/3D Cd-$ZnIn_{2.2}S_y$ heterostructure as a sensing platform for ultrasensitive detection of neuron-specific enolase, Anal. Chem. 94 (50) (2022) 17396–17404, https://doi.org/10.1021/acs.analchem.2c02645.
[17] J. Chen, J. Zhao, R. Feng, H. Ma, H. Wang, X. Ren, Q. Wei, H. Ju, Competitive photoelectrochemical aptamer sensor based on a Z-scheme Fe_2O_3/g-C_3N_4 heterojunction for sensitive detection of lead ions, J. Hazard Mater. 459 (2023), https://doi.org/10.1016/j.jhazmat.2023.132122.
[18] X. Ren, J. Chen, C. Wang, D. Wu, H. Ma, Q. Wei, H. Ju, Photoelectrochemical sensor with a Z-scheme Fe_2O_3/CdS heterostructure for sensitive detection of mercury ions, Anal. Chem. 95 (46) (2023) 16943–16949, https://doi.org/10.1021/acs.analchem.3c03088.
[19] L. Deng, F. Ma, M. Yang, X. Li, X. Chen, A halide perovskite/lead sulfide heterostructure with enhanced photoelectrochemical performance for the sensing of alkaline phosphatase (ALP), Chem. Commun. 59 (10) (2023) 1361–1364, https://doi.org/10.1039/d2cc06142b.
[20] H. Wang, B. Zhang, Y. Tang, C. Wang, F. Zhao, B. Zeng, Recent advances in bismuth oxyhalide-based functional materials for photoelectrochemical sensing, TrAC, Trends Anal. Chem. 131 (2020) 116030, https://doi.org/10.1016/j.trac.2020.116020.
[21] S.-Y. Yu, L. Zhang, L.-B. Zhu, Y. Gao, G.-C. Fan, D.-M. Han, G. Chen, W.-W. Zhao, Bismuth-containing semiconductors for photoelectrochemical sensing and biosensing, Coord. Chem. Rev. 393 (2019) 9–20, https://doi.org/10.1016/j.ccr.2019.05.008.
[22] Z. He, S. Liu, Y. Zhong, D. Chen, H. Ding, J. Wang, G. Du, G. Yang, Q. Hao, Preparation of $BiPO_4$/graphene photoelectrode and its photoelectrocatalytic performance, Chin. J. Catal. 41 (2) (2020) 302–311, https://doi.org/10.1016/s1872-2067(19)63520-5.
[23] H. Yang, J. Li, Q. Su, B. Wang, Z. Zhang, Y. Dai, Y. Li, L.a. Hou, Construction of Bi_2MoO_6/$CoWO_4$ Z-scheme heterojunction for high-efficiency photocatalytic degradation of norfloxacin under visible light: performance and mechanism insights, Chem. Eng. J. 470 (2023) 144139, https://doi.org/10.1016/j.cej.2023.144139.

[24] H. Hao, D. Lu, Q. Wang, Photoelectrochemical study on charge separation mechanisms of Bi_2WO_6 quantum dots decorated g-C_3N_4, Int. J. Hydrogen Energy 43 (18) (2018) 8824–8834, https://doi.org/10.1016/j.ijhydene.2018.03.192.
[25] N. Yang, S. Zhang, Y. Xiao, Y. Qi, Y. Bao, P. Xu, S. Jin, F. Zhang, Insight into the key restriction of $BiVO_4$ photoanodes prepared by pyrolysis method for scalable preparation, Angew. Chem., Int. Ed. (2023) e202308729, https://doi.org/10.1002/anie.202308729.
[26] M. Yu, Y. Tang, Y. Liao, W. He, X.-x. Lu, X. Li, Defect-designed Mo-doped $BiVO_4$ photoanode for efficient photoelectrochemical degradation of phenol, J. Mater. Sci. Technol. 165 (2023) 225–234, https://doi.org/10.1016/j.jmst.2023.06.002.
[27] S. Wang, P. Chen, Y. Bai, J.H. Yun, G. Liu, L. Wang, New $BiVO_4$ dual photoanodes with enriched oxygen vacancies for efficient solar-driven water splitting, Adv. Mater. 30 (20) (2018) e1800486, https://doi.org/10.1002/adma.201800486.
[28] Q. Zeng, S. Wang, Y. Qian, M. Yang, L. Lu, Photoelectrochemical immunosensor for HER2 detection based on $BiVO_4$-Bi_2S_3 heterojunction as photoactive material and CdS as signal probe, Microchim. Acta 190 (2) (2023), https://doi.org/10.1007/s00604-022-05628-4.
[29] E.A. Bondarenko, E.A. Streltsov, M.V. Malashchonak, A.V. Mazanik, A.I. Kulak, E. V. Skorb, Giant incident photon-to-current conversion with photoconductivity gain on nanostructured bismuth oxysulfide photoelectrodes under visible-light illumination, Adv. Mater. 29 (40) (2017), https://doi.org/10.1002/adma.201702387.
[30] M. Wang, S. Zeng, A.R. Woldu, L. Hu, $BiVO_4$/Bi_2S_3 Z-scheme heterojunction with MnO_x as a cocatalyst for efficient photocatalytic CO_2 conversion to methanol by pure water, Nano Energy 104 (2022), https://doi.org/10.1016/j.nanoen.2022.107925.
[31] Y. Liu, Z. Cai, L. Sheng, M. Ma, X. Wang, A magnetic relaxation switching and visual dual-mode sensor for selective detection of Hg^{2+} based on aptamers modified Au@Fe_3O_4 nanoparticles, J. Hazard Mater. 388 (2020), https://doi.org/10.1016/j.jhazmat.2019.121728.
[32] J. Xu, Y. Zhang, X. Zhu, G. Ling, P. Zhang, Two-mode sensing strategies based on tunable cobalt metal organic framework active sites to detect Hg^{2+}, J. Hazard Mater. 465 (2024) https://doi.org/10.1016/j.jhazmat.2024.133424.
[33] X. Gao, H.B. Wu, L. Zheng, Y. Zhong, Y. Hu, X.W. Lou, Formation of mesoporous heterostructured $BiVO_4$/Bi_2S_3 hollow discoids with enhanced photoactivity, Angew. Chem., Int. Ed. 53 (23) (2014) 5917–5921, https://doi.org/10.1002/anie.201403611.
[34] Z. Wei, M. Kayceety, A. Price, K. Wei, Q. Luo, S. Thanneeru, S. Sun, J. He, Polymer N-Heterocyclic Carbene (NHC) Ligands for Silver nanoparticles, ACS Appl. Mater. Interfaces 14 (49) (2022) 55227–55237, https://doi.org/10.1021/acsami.2c17706.
[35] N. Kurnaz Yetim, N. Aslan, M.M. Koç, Structural and catalytic properties of Fe_3O_4 doped Bi_2S_3 novel magnetic nanocomposites: p-Nitrophenol case, J. Environ. Chem. Eng. 8 (5) (2020) 104258, https://doi.org/10.1016/j.jece.2020.104258.
[36] L. Cao, Y. Zhou, L. Gao, H. Yin, M. Zhang, H. Zhang, P. Ju, K. Dou, S. Ai, Ascorbic acid induced the improved oxygen vacancy defects of $Bi_4O_5Br_2$ and its application on photoelectrochemical detection of DNA Demethylase MBD2 with improved detection sensitivity, Small (2023), https://doi.org/10.1002/smll.202306365.